Honda Research Institute EU
Honda Research Institute Europe GmbH
https://www.honda-ri.de/

Effect of endwall contouring on performance of ultra-low aspect ratio transonic turbine inlet guide vanes

Toyotaka Sonoda, Martina Hasenjäger, Toshiyuki Arima, Bernhard Sendhoff

2009

Preprint:

This is an accepted article published in Journal of Turbomachinery. The final authenticated version is available online at: https://doi.org/[DOI not available]

Effect of End Wall Contouring on Performance of Ultra-Low Aspect Ratio Transonic Turbine Inlet Guide Vanes

Toyotaka Sonoda
Honda R&D Co.,
Aircraft Engine R&D Center,
1-4-1 Chuo, Wako-shi,
Saitama 351-0193, Japan

Martina Hasenjäger
Honda Research Institute Europe GmbH,
Carl-Legien-Strasse 30,
D-63073 Offenbach/Main, Germany
e-mail: martina.hasenjaeger@honda-ri.de

Toshiyuki Arima
Honda R&D Co.,
Fundamental Technology Research Center,
1-4-1 Chuo, Wako-shi,
Saitama 351-0193, Japan

Bernhard Sendhoff
Honda Research Institute Europe GmbH,
Carl-Legien-Strasse 30,
D-63073 Offenbach/Main, Germany
e-mail: bs@honda-ri.de

In our previous work on ultralow-aspect ratio transonic turbine inlet guide vanes (IGVs) for a small turbofan engine (Hasenjäger et al., 2005, "Three Dimensional Aerodynamic Optimization for an Ultra-Low Aspect Ratio Transonic Turbine Stator Blade," ASME Paper No. GT2005-68680), we used numerical stochastic design optimization to propose the new design concept of an extremely aft-loaded airfoil to improve the difficult-to-control aerodynamic loss. At the same time, it is well known that end wall contouring is an effective method for reducing the secondary flow loss. In the literature, both "axisymmetric" and "nonaxisymmetric" end wall geometries have been suggested. Almost all of these geometric variations have been based on the expertise of the turbine designer. In our current work, we employed a stochastic optimization method—the evolution strategy—to optimize and analyze the effect of the axisymmetric end wall contouring on the IGV's performance. In the optimization, the design of the end wall contour was divided into three different approaches: (1) only hub contour, (2) only tip contour, and (3) hub and tip contour, together with the possibility to observe the correlation between hub/tip changes with regard to their joint influence on the pressure loss. Furthermore, three-dimensional flow mechanisms, related to a secondary flow near the end wall region in the low-aspect ratio transonic turbine IGV, was investigated, based on the above optimization results. A design concept and secondary flow characteristics for the low-aspect ratio full annular transonic turbine IGV is discussed in this paper.
[DOI: 10.1115/1.2813015]

Introduction

In order to meet increasing technical demands on small gas turbine engines, we investigate the use of low-aspect-ratio (AR) blades for which the influence of secondary flow losses on the turbine stage efficiency is very large, especially for the high-pressure turbine (HPT). A lot of literature that is concerned with the secondary flow mechanisms has been published so far. Some models for the spatial secondary flow have been obtained from flow visualization, e.g., Klein [1], Langston et al. [2,3], Sieverding and Van den Bosch [4], Sonoda [5], and Wang et al. [6]. These models are almost all based on low speed and especially on linear cascades. As an example, Fig. 1 shows the author's result obtained with low speed for a linear cascade, i.e., a high-AR turbine cascade. It is well known that the transverse (circumferential) static pressure gradient from pressure surface (PS) to suction surface (SS) plays an important role. The basic behavior of the vortex motion in Fig. 1 agrees with the previously reported results. Furthermore, according to the total pressure measurement downstream of the trailing edge (TE), the losses related to the horseshoe vortices: H_p and H_s are smaller than the loss related to the vortex IV. However, from an engineering point of view the following question must be raised: Is the secondary flow model obtained from the linear cascade (high aspect ratio) still applicable to an annular low-AR high speed cascade, especially for an ultralow-AR annular transonic turbine inlet guide vane (IGV) cascade?

Regarding the secondary flow control technique, airfoil lean and/or bowed stacking has been used especially in a low-pressure turbine for large-midsize engines. Another important method for secondary flow reduction is end wall contouring. There are two contouring types: with and without axis symmetry. In this research, we focus on the axisymmetric contouring because it is relatively simple and leads to a lower manufacturing cost than the nonaxisymmetric type.

Deich et al. [7] reported an optimal contraction ratio as a function of the AR. Ewen et al. [8] incorporated a tip contouring in the stator of a single-stage research turbine. They pointed out the importance of improved rotor inlet flow conditions. Morris and Hoare [9] showed a large reduction in the total pressure loss in the half span adjacent to the flat wall and no change around the contouring side in their plain cascade. Kopper et al. [10] tested a linear cascade of turbine vanes with and without end wall contouring. The aerodynamic loading was reduced around the frontal part of the vane, and the point of minimum pressure was moved closer to the TE. The adverse pressure gradient from the point of minimum pressure to the TE was reduced for the flat wall, but was increased for the end wall contouring. The mass averaged data showed that the contouring reduced the overall loss by 17% compared to the parallel walls. The most significant loss reduction occurred at the planar wall.

Regarding the end wall contouring of the low speed annular cascade, Boletis [11] showed that the transverse pressure gradient was significantly decreased at the frontal part, while the radial pressure gradient imposed by the blade design was counteracted by the creation of a low static pressure region at the tip end wall suction side corner. Also, the importance of the radial gradient was reported. The AR of the vane was 0.6.

Regarding the end wall contouring of the transonic annular and/or supersonic cascade, Haas [12] showed that the contoured stators had higher loss near the tip contouring side and lower loss

Contributed by the International Gas Turbine Institute of ASME for publication in the JOURNAL OF TURBOMACHINERY. Manuscript received July 23, 2007; final manuscript received August 20, 2007; published online November 10, 2008. Review conducted by David Wisler. Paper presented at the ASME Turbo Expo 2007: Land, Sea and Air (GT2007), Montreal, QB, Canada, May 14–17, 2007.

Downloaded 19 Dec 2008 to 202.33.79.26. Redistribution subject to ASME license or copyright; see http://www.asme.org/terms/Terms_Use.cfm

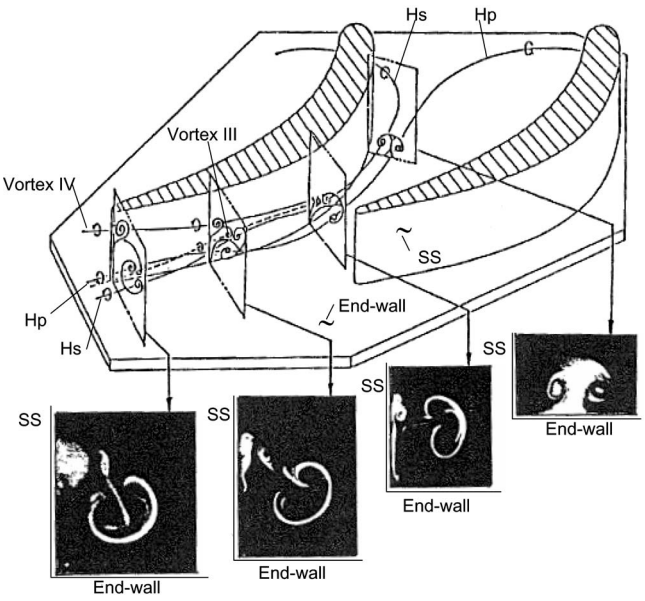

Fig. 1 Secondary flow model for a low speed and high-AR turbine blade (obtained from Sonoda [5])

near the hub than the cylindrical stator. He also pointed out the increase of the mass flow rate for the contoured stator because of differences in the physical throat areas. Moustapha and Williamson [13] reported on the effect of the tip end wall contouring for annular transonic and/or supersonic cascades. They showed improvement of the loss at the hub region, while the loss was increased at the contoured tip side. They also noticed a significant underturning region near the hub side.

As we mentioned already, the aerodynamic characteristics of end wall contouring for subsonic speed has been thoroughly investigated. However, much less work has concentrated on transonic end wall contouring, and the corresponding secondary flow mechanisms remain unclear.

Therefore, the main objective of this research is to investigate the effect of three types of end wall contouring: (1) only hub contour, (2) only tip contour, and (3) hub and tip contour on the aerodynamic performance of the ultralow-AR transonic turbine IGV. Furthermore, we investigate the secondary flow mechanisms, particularly whether there is a difference between the secondary flow model obtained from the low speed and from the linear cascade conditions.

Ultralow-Aspect-Ratio Transonic Turbine Inlet Guide Vanes. Figure 2 shows the meridional passage of the ultralow-aspect-ratio transonic turbine IGVs. The vane used in the present investigation is an IGV in a single-stage HPT for a small turbofan engine that has been installed in a small business jet. The corrected mass flow rate is relatively low at 0.84 kg/s, and the exit Mach number and flow angle are 1.04 and 72.8 deg at midspan height, respectively. The Reynolds number Re based on the actual (true) chord at midspan height is 3,500,000. The number of blades (NB) was set at 8 in order to avoid the first resonance with a downstream rotor within the operating range, keeping the vane solidity constant. This leads to an "ultralow-AR vane" of 0.21 (ratio of exit passage height to actual chord at hub), and the passage contraction ratio is 0.52. These parameters correspond to the optimized contraction line proposed by Deich et al. [7]. Constrained by manufacturing costs, e.g., due to necessary cooling, the blade geometry is defined by only two cross sections, the hub and the tip section. Linear interpolation between these two sections is used to define the remaining blade geometry. The stator blade is circumferentially leaned by 14 deg in order to suppress the development of a secondary flow near the hub end wall. The blade axial solidity is constant along the span, and it is 0.76. Zweifel's loading coefficient Zw is 0.80. The axial coordinate $X=0$ roughly corresponds to the TE of the ultralow-AR vane and $X=+0.13$ refers to the leading edge (LE) location downstream of the rotor blade, called Station 2. In the following, we will refer to this blade and passage as the base line vane and base line passage, respectively, particularly when we compare it to the optimization results.

Design Optimization With Evolutionary Algorithms

Evolutionary algorithms [14] are a class of stochastic optimization algorithms whose use in design optimization problems is well established by now [15]. These algorithms are inspired by principles of evolutionary biology and make use of a population of individuals—each individual representing a specific design—to search the design space for the optimum solution. Typical operators applied during evolutionary optimization are selection to direct the search to promising regions of the search space, recombination to combine promising features of known solutions, and mutation to introduce some random changes of the solutions.

In our approach to aerodynamic design optimization, we use a special variant of evolutionary algorithms, namely, an evolution strategy (ES) with covariance matrix adaptation (CMA) [16]. The basic idea of CMA-ES is to make maximum use of the information contained in the search history for a self-adaptation of the search direction that is defined in terms of the covariance matrix of a normal distribution from which new tentative solutions or individuals are drawn. Thereby, the population size is decoupled from the dimension of the search space.

Especially the latter feature is indispensable in aerodynamic design optimization, which, in general, is characterized by a fundamental conflict: On the one hand, the design space easily becomes relatively high dimensional. As a consequence, a large

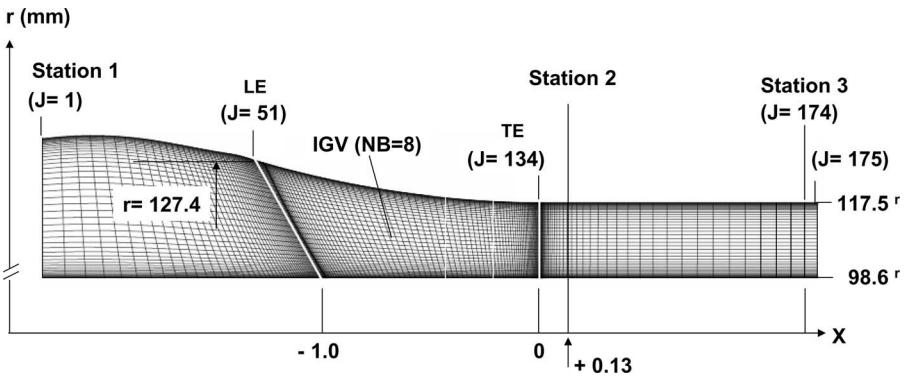

Fig. 2 Meridional passage of an ultralow-AR IGV

Downloaded 19 Dec 2008 to 202.33.79.26. Redistribution subject to ASME license or copyright; see http://www.asme.org/terms/Terms_Use.cfm

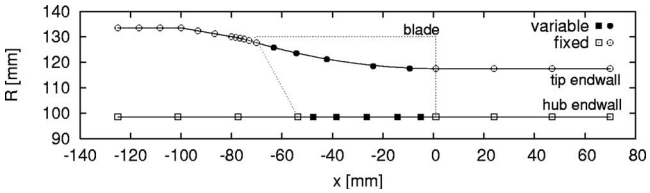

Fig. 3 Passage modeling

number of different designs have to be evaluated during optimization. On the other hand, however, the evaluations typically involve computational fluid dynamics (CFD) based flow analyses and are thus highly challenging tasks with respect to the necessary computational resources as well as with respect to the time requirements. As a result, only a limited number of evaluations can be afforded.

Geometrical Models. A crucial point in design optimization is the parametric model of the geometry that will be optimized since this determines the design space, i.e., the set of all possible designs and the topology of the design or quality space. There are a number of requirements for the parametric model:

- flexibility: the model must be flexible enough to represent a wide variety of different designs
- compactness: the number of parameters describing the model must be low enough to allow for reasonable convergence times of the optimization algorithm
- locality: variations of a single model parameter should result in only local variations of the model and should not affect the global model shape

A good choice to fulfil these requirements is to use nonuniform rational *B*-spline (NURBS) models [17] to represent geometrical models in design optimization. In general, NURBS models are defined by (i) a set of control points, (ii) a weight for each control point, and (iii) a single knot vector in the case of NURBS curves or two knot vectors in the case of NURBS surfaces, one for each parameter. Usually not all of these parameters are subject to optimization. We should note that the NURBS representation only fulfils the flexibility condition if the number of control points is sufficiently large.

Passage Model. The passage model consists of two open nonuniform *B*-spline curves, one curve modeling the hub end wall and the other curve modeling the tip end wall (Fig. 3). As parameters in the optimization, we considered a subset of the control points of the *B*-spline curves and allowed them to vary in both the radial and the axial coordinate. Note that allowing the axial control point position to vary is not redundant but introduces a flexibility into the model that is worthwhile in terms of possible performance gains.

The hub end wall is defined by 13 control points shown as squares in Fig. 3. Only 5 of these 13 control points are used as design variables in the optimization. Variation of the control point position is possible in both the x coordinate of the control point as well as in the y coordinate. This gives us ten variable parameters to model the hub passage contour. The tip end wall is defined by 21 control points shown as circles in Fig. 3. Only the five control points shown as filled circles in Fig. 3 are variable. Again, variation of the control point position during optimization is possible in both the x coordinate of the control point as well as in the y coordinate. So, we have ten variable parameters to model the casing passage contour. In both end wall models, the knot vectors of the nonuniform *B*-spline curves are fixed and not subject to optimization.

Objective Function in the Optimization. The performance measure f of a specific passage design is given by the single objective of minimizing the mass averaged pressure loss ω of the stator. Additionally, we use range constraints on (i) the β_2 outflow angle and (ii) the mass flow rate. The outflow angle is constrained to lie in the range of $\delta\beta_2$ around the design value $\beta_{2\text{design}}$. In the same way, the mass flow rate is constrained to lie in the range of $\delta\dot{m}$ around the design value $\dot{m}_{\text{design}}$. The constraints are included in the objective function in the form of a weighted sum of penalty terms. Thus, the objective function for the optimization is given by

$$f = \omega + \sum_{i=1}^{2} w_i t_i^2 \rightarrow \min \tag{1}$$

with

$$t_1 = \max(0, |\beta_{2,\text{design}} - \beta_2| - \delta\beta_2)$$

$$t_2 = \max(0, |\dot{m}_{\text{design}} - \dot{m}| - \delta\dot{m})$$

We used the following design values, tolerances, and weights in the fitness function:

$$\beta_{2,\text{design}} = 72.0 \text{ deg}$$

$$\delta\beta_2 = 0.5 \text{ deg}$$

$$w_1 = 10^{19}$$

$$\dot{m}_{\text{design}} = 0.84 \text{ kg s}^{-1}$$

$$\delta\dot{m} = 0.017 \text{ kg s}^{-1}$$

$$w_2 = 10^5$$

Here, the averaged pressure loss ω is estimated far downstream at outlet Station 3 for considering mixing losses. The mass flow rate $\dot{m}$ and the outflow angle β_2 are estimated at outlet Station 2, just downstream of the TE (see Fig. 2 for the location of the outlet stations). The design outflow angle β_2 of 72.0 deg used in the optimization is slightly different from that in the actual turbine aerodynamic design of 72.8 deg. The reason will be explained in the section on the reliability of 3D Navier–Stokes solver. The geometrical model of the base line passage that was used to initialize the optimization lies within the feasible region of the design space. According to Eq. (1), only violated constraints contribute to the objective function. The weights w_1 and w_2 on the constraints are constant during optimization and are chosen such that the contribution of a violated constraint by far outweighs the contribution of the objective ω in order to quickly drive the search back into the feasible region.

Flow Solver. For the simulation of the fluid dynamic properties of the passage designs, we used the parallelized 3D in-house Navier-Stokes flow solver HSTAR3D (see Ref. [18]), with Wilcox's k-ω two equation model [19]. Prior to optimization, we performed CFD calculations of the base line geometry to determine the necessary grid size for a high resolution of the boundary layer development. The computational grid consisted of $175(J) \times 52(K) \times 64(L) = 58,2400$ cells. The average y^+ of the first grid point from the wall is about 1.5 for all calculations. The computation time for one flow analysis with this grid depends on the passage geometry. It takes roughly 1 h on two AMD Opteron 2 GHz dual processors.

Optimization Algorithm. A flowchart of our optimization environment is given in Fig. 4. The basic setup is governed by two parallelization levels. On the first level, the evolutionary operators are used to generate the offspring population, i.e., the new blade designs. In our algorithm, we do not use a recombination procedure. Instead, changes are induced during mutation by adding normally distributed random numbers to the design parameters that are subject to optimization. As noted before, the covariance matrix

Downloaded 19 Dec 2008 to 202.33.79.26. Redistribution subject to ASME license or copyright; see http://www.asme.org/terms/Terms_Use.cfm

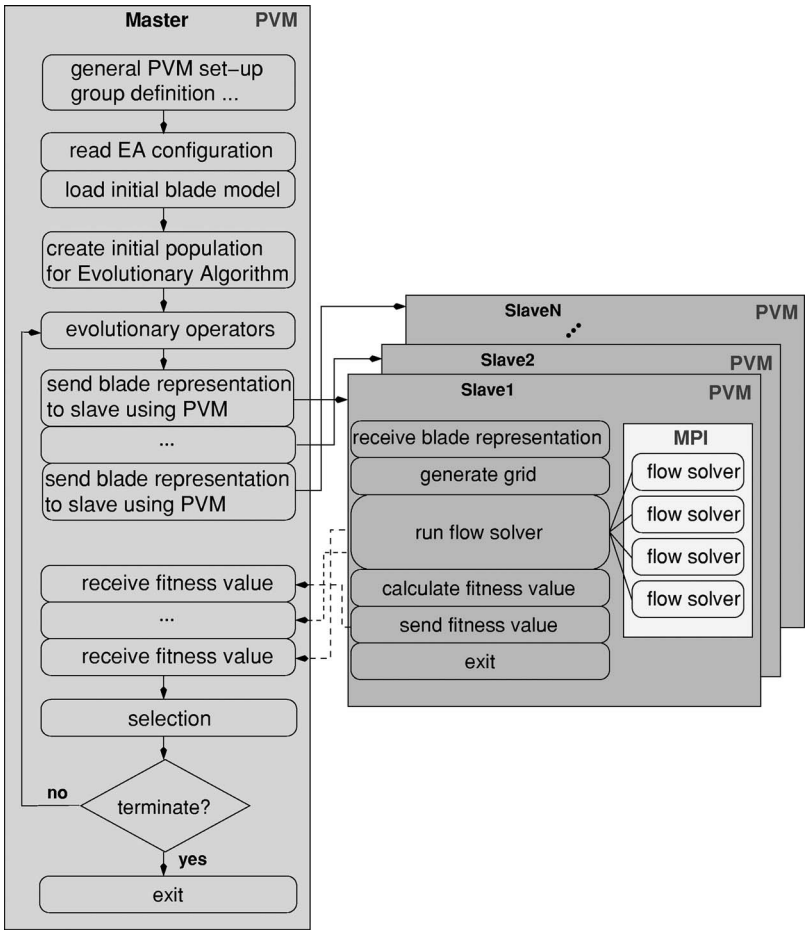

Fig. 4 Flowchart of optimization environment

of the normal distribution is adapted to the local topology of the search space. The λ offspring individuals—here, λ denotes the offspring population size—are evaluated in parallel by sending each blade representation to separate slave processes using the parallel virtual machine (PVM) library [20]. The slave processes generate the computational grid and run the flow solver using an additional set of four processes, which are distributed using message passing interface (MPI) [21]. This constitutes the second level of parallelization. The slave processes calculate the objective function (Eq. (1)) and send the resulting quality value back to the master process. The master collects the quality values for all λ individuals or blade designs. Next, the best μ designs are selected from these λ individuals to become the parent population of the next generation. In evolutionary algorithms, this type of "deterministic" selection method is written as the (μ,λ) selection. The evolutionary cycle proceeds with the creation of the next offspring generation as long as the stop criteria are not met. Ideally, stop criteria should depend on the expected performance gain and should stop the optimization when this value falls below a certain threshold. In reality, the optimization is often stopped because of time constraints.

For the results presented in this paper, a (μ,λ) CMA-ES with $\mu=1$ parent individual and $\lambda=10$ offspring individuals was used. The optimization was initialized with a geometry similar to the base line passage. All offspring individuals were evaluated in parallel. For this, we used a 40 processor computing cluster: ten parallel processes were running in the first level of parallelization and each of these spawned four processes in the second level of parallelization.

Results and Discussions

Reliability of 3D Navier-Stokes Flow Solver. It is very important to estimate the reliability of the 3D flow solver used in this turbine end wall optimization in advance. So far, the flow solver has been successfully used for compressor and turbine blades. For example, the 3D flow solver with a low Reynolds k-ε turbulence model proposed by Chien [22] has been successfully applied to the compressor blade of NASA Rotor67 and 37 [18].

A 2D version of the flow solver with the same turbulence model has also been applied successfully to a transonic turbine cascade [23]. In this research and in our previous work [24], the Wilcox's k-ω model [19] has been used for the 3D transonic turbine blade for an easier determination of the length from the wall. However, a precise validation with the new model has not been done yet. The reason is that it is very expensive and time consuming to prepare the validation data for the 3D transonic annular turbine cascade. Therefore, we estimate the reliability as far as possible based on data obtained from a transonic turbine stage rig shown in Fig. 5. We should note that the following data were not measured for the purpose of validation and that errors are inherent.

The comparison of EXP and CFD was carried out, focusing on the oil flow visualization and the loss and the exit flow angle distributions at the nominal IGV exit plane: Station 2, i.e., 7 mm downstream of the TE (corresponding to 0.13 axial chord downstream of the TE). The test facility was designed for full size testing of the HPT, and the test was carried out under the "cold" condition at the design corrected mass flow rate. Therefore, the axial gap between the base line IGV and the rotor was newly

Downloaded 19 Dec 2008 to 202.33.79.26. Redistribution subject to ASME license or copyright; see http://www.asme.org/terms/Terms_Use.cfm

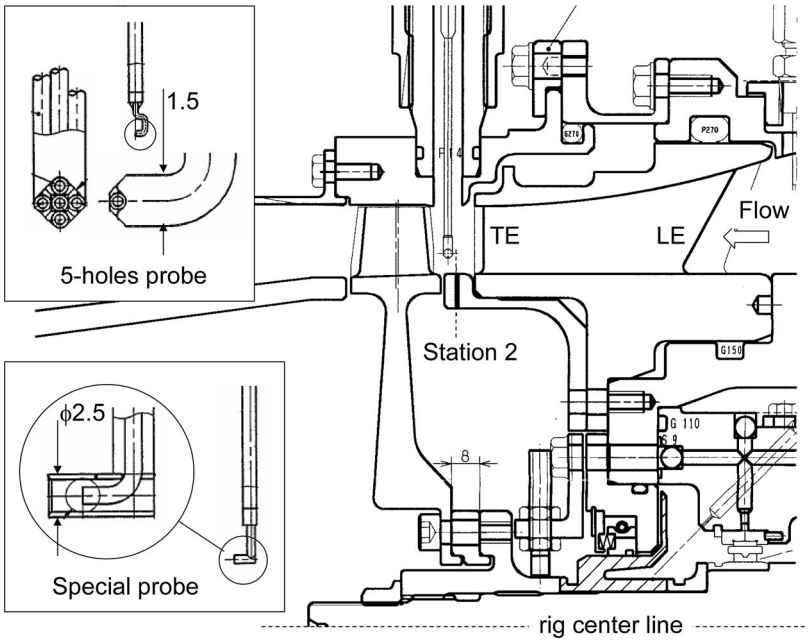

Fig. 5 Experimental apparatus for IGV wake traverse measurement at Station 2, using a transonic turbine stage rig

extended to be able to do the traverse measurement radially and circumferentially. However, there are no static pressure taps on the IGV surface because this rig has been used for the estimation of the stage performance, as already mentioned above.

The traverse was performed using two types of probes. One is a special probe that is not sensitive for the flow angle variation, as shown in Fig. 5. This was mainly used for total pressure measurement. The other one is a five-hole probe for the flow angle measurement, also shown in Fig. 5. Regarding the total pressure measurement, the circumferential increment is 2 deg to the 1 pitch (45 deg: NB=8), and about 1 pitch measure was done. The radial positions were seven sections, so the total number of measure points is 161 points (23×7).

In this research, the total pressure loss coefficient is not defined in terms of the exit dynamic head as the denominator, but in terms of the inlet total pressure. There are two reasons for this: firstly, a large circumferential variation (not negligibly small) of the static pressure value was observed on the outer casing downstream of the IGV-TE (at Station 2) (not shown here). This may be due to a narrow gap between the IGV and a rotor. The second reason is that as far as CFD results are concerned, there is no linear distribution at Station 2 (not shown here). Therefore, we decided to use the inlet total pressure, instead of the exit dynamic head, in order to achieve a high accuracy on the data processing.

For the flow angle measurement using the five-hole probe, the radial flow component was neglected. The traverse measurement was done with the same circumferential increment as the total pressure measurement, but the radial measurement positions were reduced from seven to five sections. The flow direction was manually determined by adjusting the pressure difference of the right hole and the left hole to be zero in the free wake region. The measurement accuracy for the total pressure loss is considered to be accurate to within ± 0.002 in the areas of relatively low total pressure loss, while the flow angle accuracy is about ± 0.5 deg.

Firstly, the oil flow visualization was carried out for the base line vane, experimentally and numerically, as shown in Fig. 6, in order to understand the overall image of the secondary flow pattern for the transonic IGV. In the experiment, this picture corre-

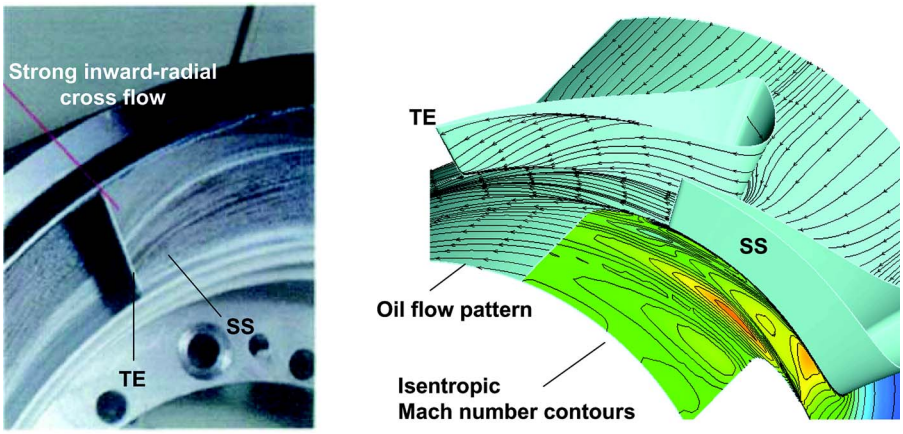

(a) EXP (NB=10) **(b) CFD (NB= 8)**

Fig. 6 Comparison of vane surface oil flow visualization for (*a*) EXP and (*b*) CFD

Downloaded 19 Dec 2008 to 202.33.79.26. Redistribution subject to ASME license or copyright; see http://www.asme.org/terms/Terms_Use.cfm

sponds to NB=10, but the tendency is almost the same as for the base line case with NB=8. There is a strong inward-radial flow near the rear part of the SS, and there is no interaction between the shock, emanating from the TE of the adjacent vane, and the SS boundary layer. It seems that the inward-radial flow pattern for the ultralow-aspect IGV is much stronger than the one for a high-AR IGV. The tendency of the oil flow pattern in CFD is almost the same as in the experiment. The end wall isentropic Mach number contours in Fig. 6(*b*) clearly show the complexity of the flow pattern. This will be discussed in the section on flow mechanism in ultra-low AR IGV.

Figure 7 (top and bottom) shows the circumferential-mass-averaged spanwise distribution of the total pressure loss and the exit flow angle, respectively. In general, a good qualitative agreement between EXP and CFD is obtained for both loss and flow angle distribution. However, the pattern of the flow angle distribution near the hub region is different from the established knowledge on the secondary flow. We observe a tendency of underturning of the exit flow angle near the hub wall. Moustapha and Williamson [13] obtained similar results for the annular cascade. They found experimentally in their annular cascade testing an overturning tendency near the hub wall in the subsonic exit Mach number. However, in the transonic and supersonic exit Mach number regions, a tendency to underturn is predominant. Unfortunately, there is no clear explanation of the reason. We will discuss this in more detail in the section on flow mechanism in ultralow-AR IGV.

Regarding the spanwise exit flow angle distribution in Fig. 7 (bottom), there is a tendency of the underestimation of about 1.0 deg at the midspan height. Therefore, in the optimization used in this paper, the design exit flow angle was set to 72 deg, instead of to 72.8 deg.

Figure 8 shows the experimental and numerical comparison of the total pressure loss contour at Station 2. As already mentioned above, there are only seven radial measurement sections for the total pressure loss, which is not sufficient for an accurate comparison between EXP and CFD. However, it seems worthwhile to highlight the unusual flow characteristics around the left of the PS circumferential area near the hub and tip wall in the experiment where the losses are never low in such an ultralow-AR transonic turbine IGV.

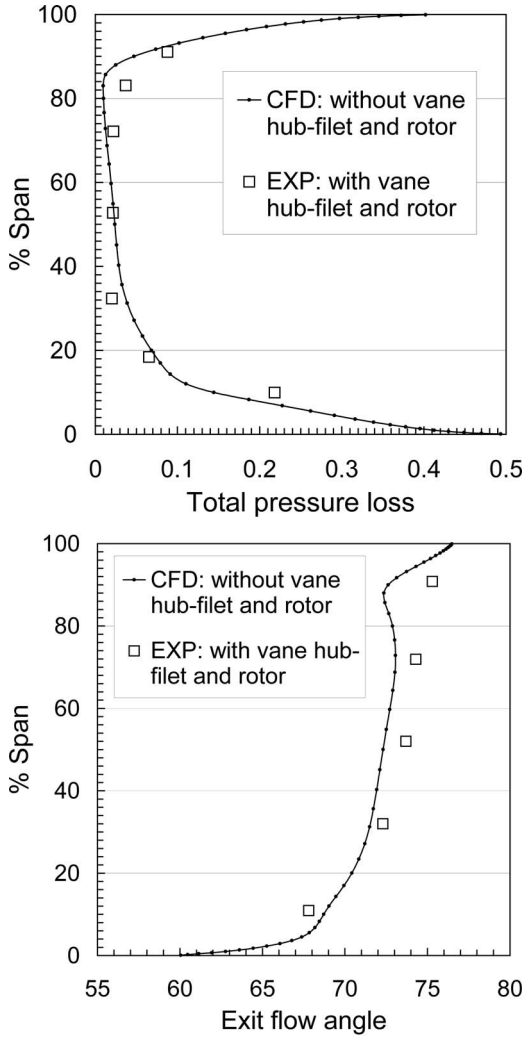

Fig. 7 Comparison of loss (top) and exit flow angle (bottom) at Station 2 for EXP and CFD

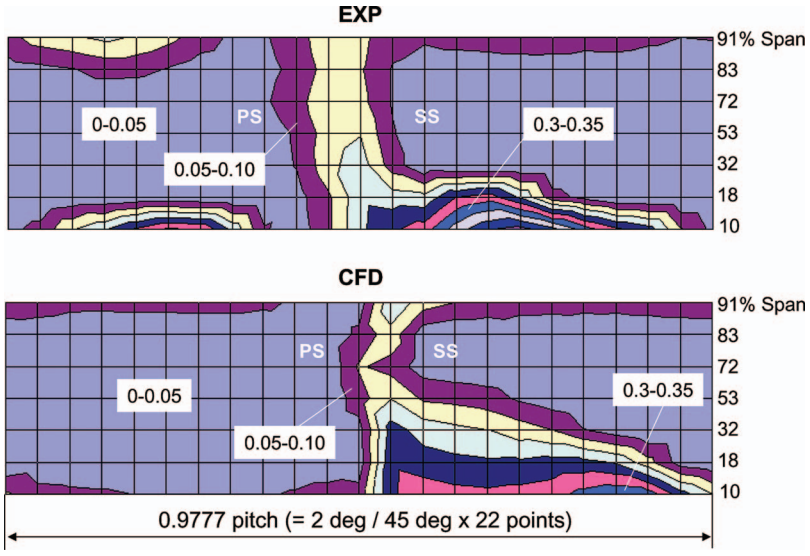

Fig. 8 Comparison of total pressure loss at Station 2 for EXP (top) and CFD (bottom); 0.05 increment

Downloaded 19 Dec 2008 to 202.33.79.26. Redistribution subject to ASME license or copyright; see http://www.asme.org/terms/Terms_Use.cfm

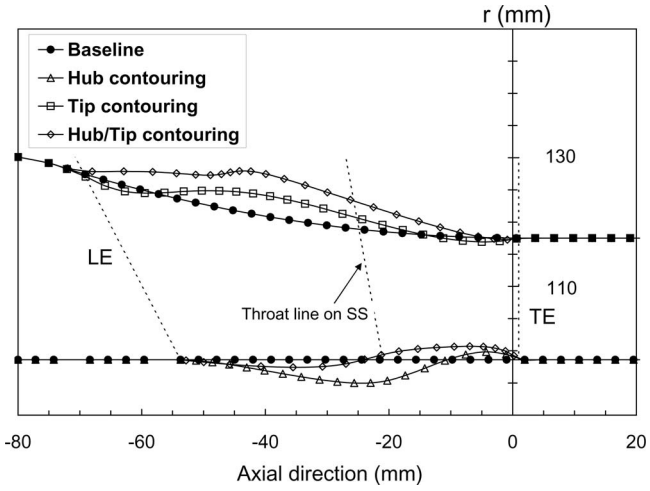

Fig. 9 Base line and optimized three passages

Comparing the wake pattern in the EXP and CFD in more detail, the wake mixing process in CFD around the wake-free region at 72% of span height is not established. At the same time, a qualitative agreement is obtained for the tip region only. A possible reason for the different quality for the hub and tip regions may be the effect of the blade filet in the EXP and the CFD. In both CFD and EXP, there is no filet on the tip end wall (under the same condition). On the contrary for the hub end wall, we only observe a filet in EXP, but not in CFD (not the same condition). The mechanism behind the unusually high loss region found around the PS in the experiment will be explained in more detail using the CFD results in the section on flow mechanism in ultralow-AR IGV.

Effect of End Wall Contouring. Figure 9 shows the passage geometries obtained from the optimization for the three cases, i.e., "hub contouring," "tip contouring," and "hub and tip contouring." The base line is also shown in the figure (black circles). In the case of hub contouring, the hub radius gradually decreases from the LE to the minimum, which is reached around the middle axial hub chord; from there, the radius gradually increases toward the TE. Furthermore, we observe an unusual hump (overshoot) of the hub line around the TE. In the case of the tip end wall contouring, a unique tip line (*S* type) is obtained. In the case of the combined hub and tip optimization, the frontal part of the passage diverges; i.e., the passage width increases and the flow is decelerated. Indeed, this is a common characteristic for all three optimization cases. The passages diverge around the frontal part and converge; i.e., the passage width decreases and the flow is accelerated around the rear part.

Figure 10 shows the isentropic Mach number distribution on the IGV surface for the three cases and the base line. Compared to the base line (Fig. 10(*a*)) in the hub contouring case (Fig. 10(*b*)), the circumferential pressure gradient, frequently called the "driving force of the secondary flow," is significantly reduced especially around the middle axial chord part and remarkably at the

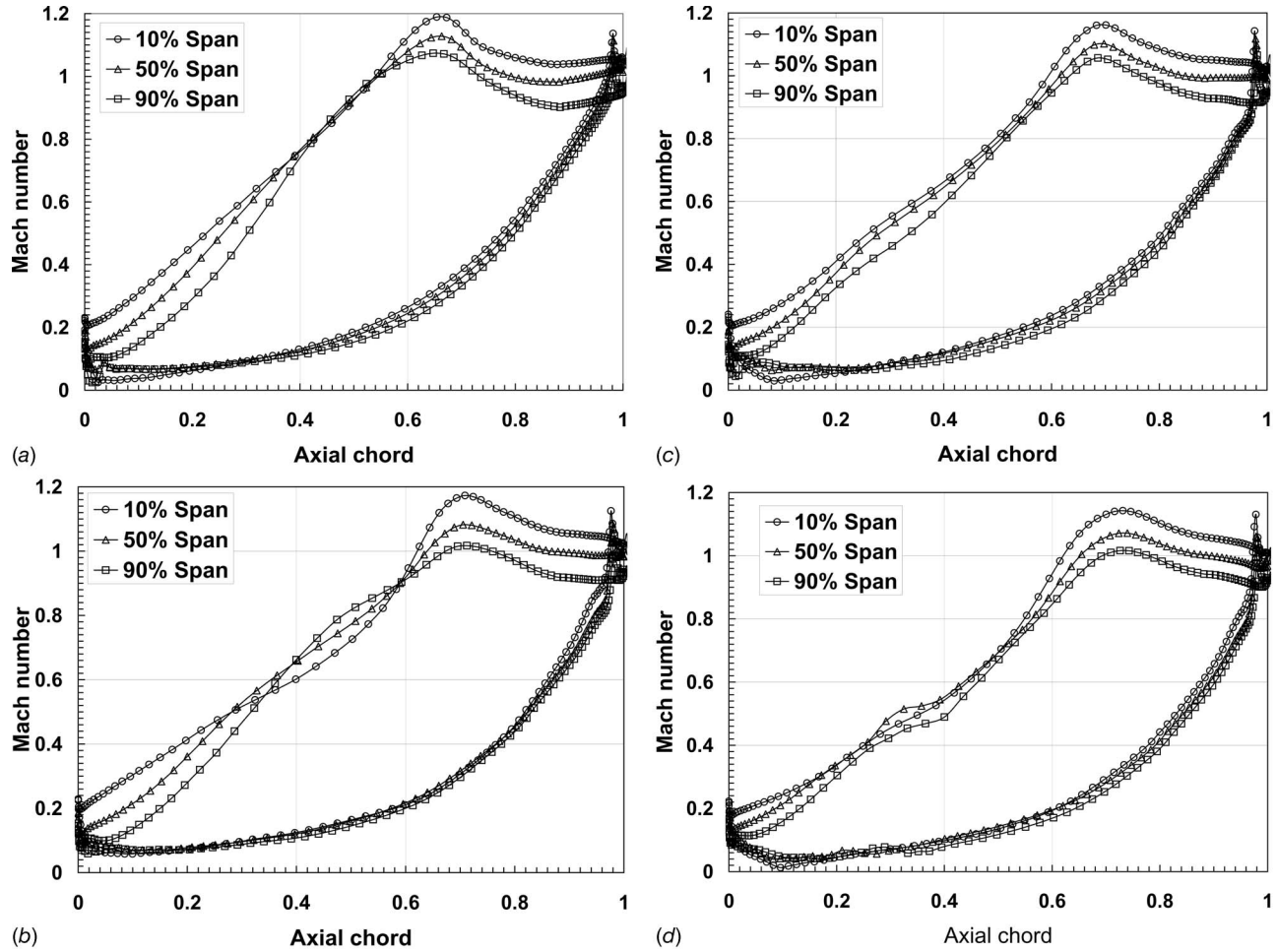

Fig. 10 Comparison of blade surface Mach number distribution for base line and three optimized passages. (*a*) base line, (*b*) hub contouring, (*c*) tip contouring, and (*d*) hub and tip contouring.

Downloaded 19 Dec 2008 to 202.33.79.26. Redistribution subject to ASME license or copyright; see http://www.asme.org/terms/Terms_Use.cfm

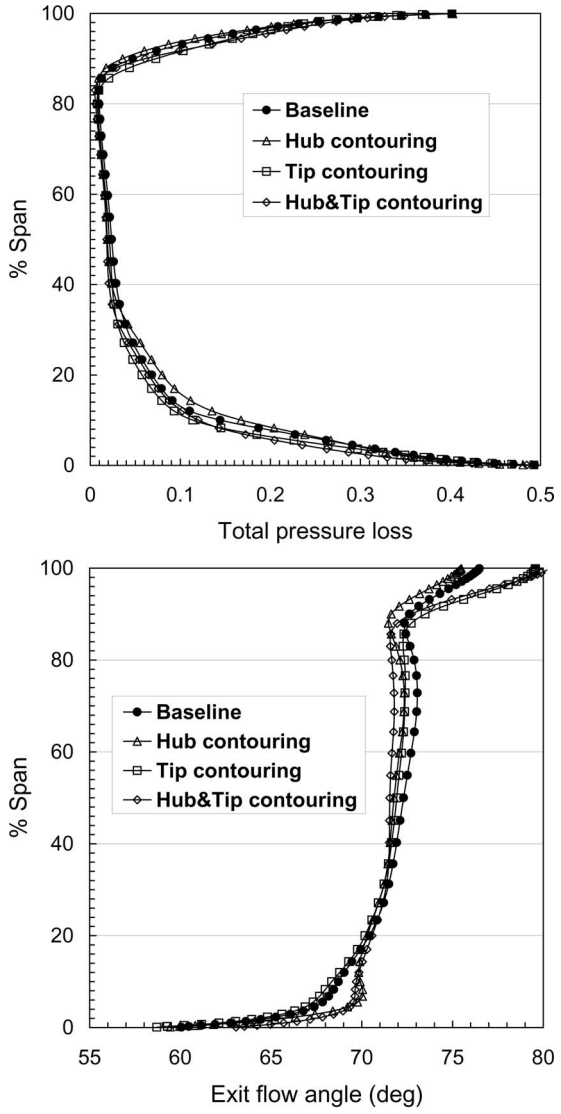

Fig. 11 Spanwise distribution of loss (top) and exit flow angle (bottom) for base line and three optimized passages

hub region (10% span). This leads to a reverse pressure gradient (P_s, tip $<P_s$, hub) around 40%–59% axial chord, which results in a reduction of the secondary flow, because the circumferential and spanwise (radial) driving forces are weaker. However, while the aerodynamic loading in the aft part is circumferentially and radially increased, the gain obtained at the middle part may disappear. This general tendency is also observed for the remaining two cases (the tip contouring and the combination of hub and tip contouring). In the case of tip contouring (Fig. 10(*c*)), there is no intersecting distribution on the SS, which is observed for the hub contouring (see Fig. 10(*b*)). In the case of the hub and tip contouring (Fig. 10(*d*)), the highest circumferential loading is observed around 80% axial chord position. Figure 11 (top) and Table 1 show the circumferential-mass averaged spanwise loss distribution and the overall mass averaged values for the three end wall contouring cases and the base line, respectively. Comparing the hub contouring with the base line, the loss between about 5% and 36% span height is worse, but for the other spanwise positions, it is improved. As a result, the overall loss reduction is 7% at Station 2 and 4% at the downstream position (Station 3), as shown in Table 1.

As already mentioned the loss at Station 2 does not include the mixing loss, but the loss at Station 3 includes both the mixing loss and the friction loss due to a large exit swirl angle (about 72 deg) from Station 2 (just downstream of IGV to Station 3) (far downstream). Here, we can see that the largest reduction rate of the loss, including the mixing and the friction losses, is achieved at Station 3 by the hub and tip contouring because all four cases have almost the same exit swirl angle and the same mass flow rate between Stations 2 and 3.

In the case of the tip end wall contouring, the minimal loss value is reached between 10% and 30% span height. Regarding the exit flow angle distribution in Fig. 11 (bottom), the underturning tendency near the hub end wall region, observed in the base line, is changed in the case of the hub contouring and the hub and tip contouring where we notice a tendency of overturning. This will be discussed in the section of flow mechanism in ultralow-AR IGV.

In summary, the optimized geometries show a lower loss than the base line. The reduction rate is 4% for the hub contouring, 5% for the tip contouring, and 10% for the combination at Station 3. Remember that we define the loss in terms of the inlet total pressure and not in terms of the exit dynamic head.

Flow Mechanism in UltraLow-Aspect-Ratio Inlet Guide Vane. Figure 12 shows the loss contours for the three optimized geometries and for the base line at Station 2. This does not correspond to an actual physical plane, but to the grid point used in CFD because this simplifies the discussion of the end wall region. Regarding the high loss region around the left side of PS, observed in the experiment (see Fig. 8, top), the CFD shows a similar loss region indexed as No. 1 in Fig. 12(*a*). Also, CFD seems to simulate the near tip region No. 2 well. Apart from the high loss region Nos. 1 and 2, there are two more high loss regions termed Nos. 3 and 4 near the hub end wall located at the SS. In the hub contouring (see Fig. 12(*b*)), the losses at Nos. 1 and 4 are reduced, but remarkably increased at No. 3. This is the reason why the loss around the 5% and 36% span is increased (see Fig. 11, top). In the case of the tip contouring (see Fig. 12(*c*)), the loss at No. 3 is dramatically decreased, but increased at Nos. 1 and 4. This is the reason why the minimal loss region is positioned at around 10%–30% span height for the tip contouring. For the combined contouring (see Fig. 12(*d*)), the loss at No. 3 is again increased, but not more than for the hub contouring. Also, the loss levels at Nos. 1 and 4 are minimal. This is one reason why the hub and tip contouring shows the maximal loss reduction.

Table 1 Performance comparison for base line and three optimized passage

Optimization cases	Total pressure loss (%)		Exit flow angle		Corrected mass flow at Station 2
	Station 2	Station 3	Station 2	Station 3	
Base line	5.92 (1.00)	10.61 (1.00)	71.8	71.7	0.84 (kg/s)
1. Hub contouring	5.53 (0.93)	10.22 (0.96)	71.5	71.6	0.85
2. Tip contouring	5.38 (0.90)	10.13 (0.95)	71.5	71.6	0.85
3. Hub and tip contouring	5.00 (0.84)	9.57 (0.90)	71.5	71.7	0.85

Downloaded 19 Dec 2008 to 202.33.79.26. Redistribution subject to ASME license or copyright; see http://www.asme.org/terms/Terms_Use.cfm

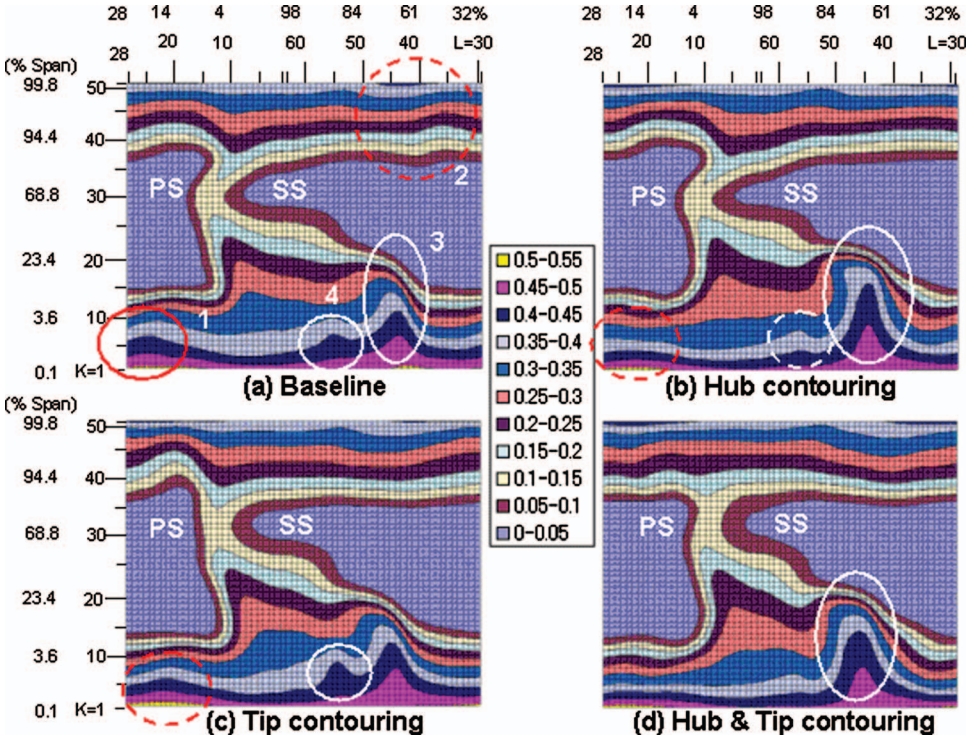

Fig. 12 Total pressure loss contour for base line and three optimized passages at Station 2

The underturning around the hub region can be mainly observed for the base line and the tip end wall contouring and is much less pronounced for the hub contouring and the hub and tip combination (see Fig. 11, bottom). The reason is that the flow angle is strongly influenced by the high loss region No. 4. Figure 13 shows the total pressure contours and the exit flow angle contours for the base line and the hub and tip contouring. In the case of the base line, there is a large underturning region corresponding to the high loss at No. 4. On the contrary, overturning is observed at around the high loss at No. 1. In the case of the hub and tip contouring, the underturning is decreased by the reduced loss at No. 4. Also, the overturning is decreased by the reduced loss at No. 1. Tentatively, we can conclude that there is a concentrated vortex around the high loss region No. 4 and the rotational direc-

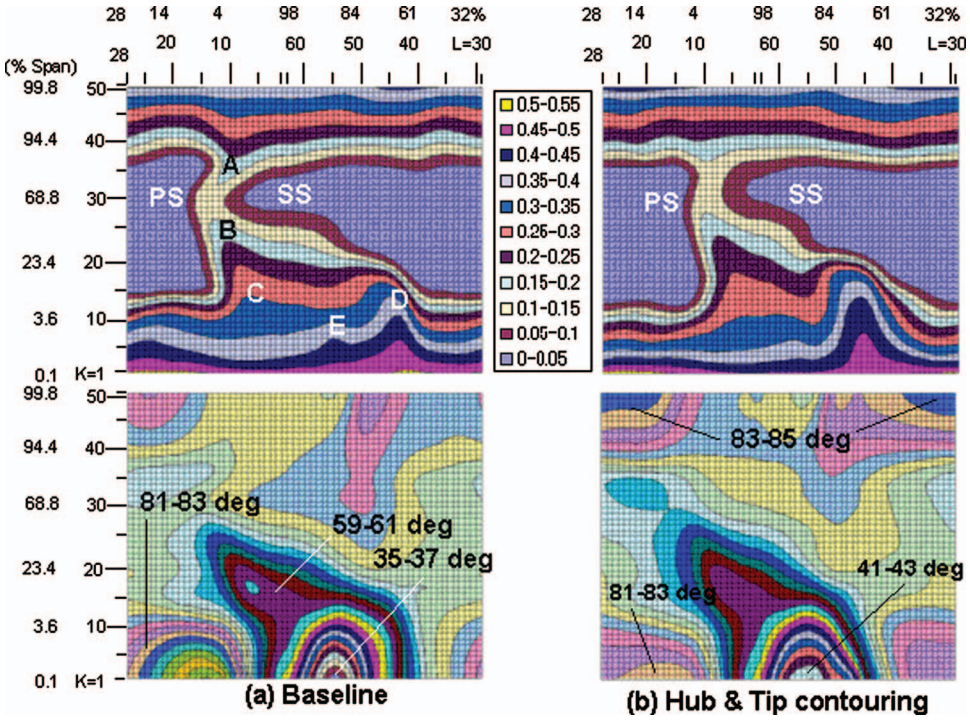

Fig. 13 Comparison of loss and exit flow angle for (*a*) base line and (*b*) hub and tip contouring

Downloaded 19 Dec 2008 to 202.33.79.26. Redistribution subject to ASME license or copyright; see http://www.asme.org/terms/Terms_Use.cfm

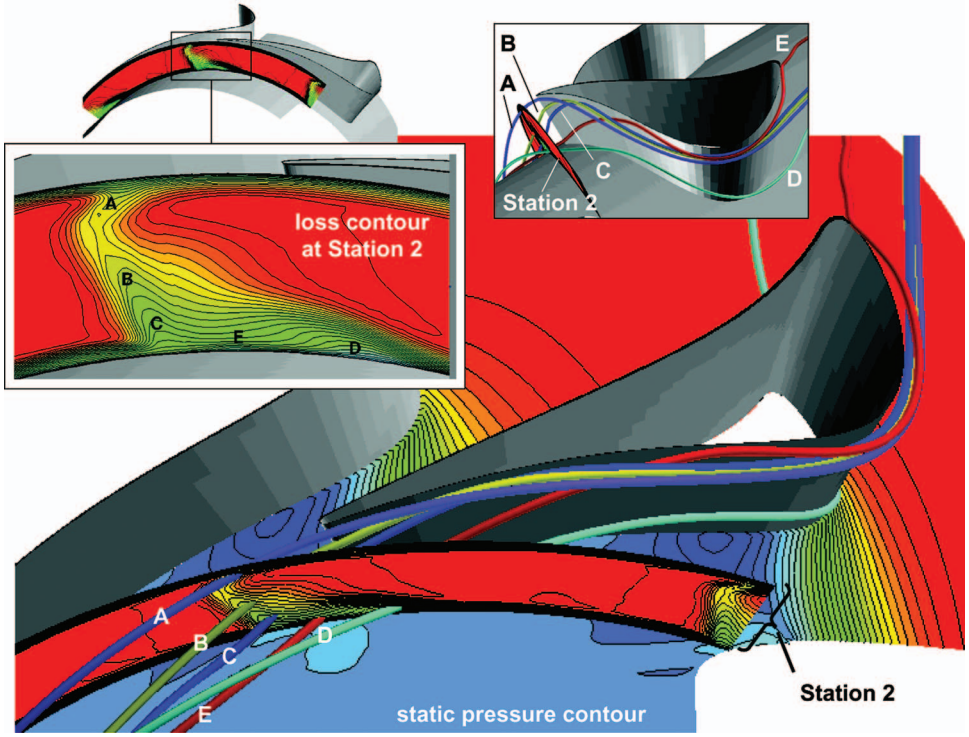

Fig. 14 Relation of high loss region and streamline for base line

tion is opposite to the H_p (see Fig. 1). However, the question remains: What are the reasons behind the high losses at Nos. 3 and 4? Therefore, a particle trace visualization was carried out. The particle was released at points A, B, C, D, and E, as shown in Fig. 13, top-left.

Figure 14 shows the results. It is very surprising that the fluid particles released at A, B, and C all come from the tip end wall, showing a spiral movement. The movement of the particles started at E seems to be independent of the A, B, C group. A particle released at D comes from the hub end wall, showing a lift-up around the middle axial chord.

Figure 15 is similar to Fig. 14, but the viewpoint is from the top in order to estimate the exit flow angle. The high loss region at E mainly causes the underturning observed near the hub region in the experiment (see Fig. 7, bottom). Also, regarding the high isentropic Mach number region downstream of the TE as shown in Fig. 6, right, there is no corresponding part in Fig. 15 (see the wall static pressure contours). Therefore, the static pressure field adja-

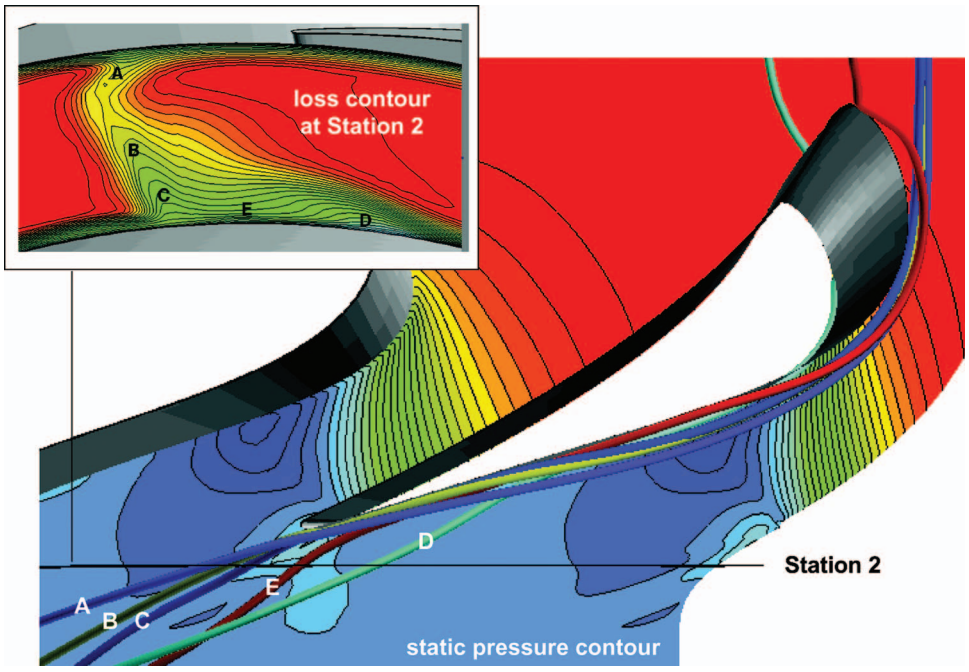

Fig. 15 Relation of high loss region and flow angle for base line

Downloaded 19 Dec 2008 to 202.33.79.26. Redistribution subject to ASME license or copyright; see http://www.asme.org/terms/Terms_Use.cfm

cent to the wall where the oil flow and the Mach number were estimated in Fig. 6 should be different from the wall static pressure due to the complex flow field, as shown in Figs. 12 and 13. A related stage testing for an optimized end wall contouring is currently being planned.

Conclusions

In this study, we employed a numerical, stochastic optimization method, namely, the ES, to investigate the effect of the end wall contouring for an ultralow-AR transonic turbine IGV in a small size HPT. The target was to investigate the effect of the end wall contouring on the aerodynamic performance and to investigate the secondary flow mechanism in order to find out whether it differs from the model obtained from the low speed and linear cascade conditions. From an aerodynamic point of view, the following conclusions can be drawn.

- The hub contouring, the tip contouring, and the hub and tip contouring all reduce the mass averaged overall loss by 4%, 5%, and 10%, respectively, as compared to the base line. Remember that we define the loss in terms of the inlet total pressure and not in terms of the exit dynamic head.
- Each contouring significantly influences the flow mechanism related to the secondary flow near the hub end wall where we observe areas of high losses and a large variation of the exit flow angle already in the base line experiments.
- The useful design concept is an aft-loaded pattern because the spanwise (radial) static pressure gradient within blade to blade is more dominant than the circumferential static pressure gradient.
- The flow mechanism in the small size full annular ultralow-AR transonic turbine IGV is different from the secondary flow model obtained from the low speed linear cascade.
- Further investigation is needed to completely clarify the secondary flow mechanism for a small size ultralow-AR transonic annular turbine cascade.

Acknowledgment

The authors are grateful to Gensuke Hoshino and Kouji Murata from the Honda R&D, who performed the test series.

Nomenclature

$\dot{m}$ = mass flow rate at Station 2
$\dot{m}_{\text{design}}$ = design mass flow rate at Station 2
P_t = total pressure
P_s = static pressure
r = radius
Re = Reynolds number, based on true (actual) chord and midheight exit flow conditions
w_i = weight in fitness function
X = coordinate related to the stator passage
y^+ = normal distance from the wall
Zw = Zweifel loading coefficient
β_2 = exit flow angle at Station 2
$\beta_{2,\text{design}}$ = design value of the exit flow angle at Station 2
$\delta\beta_2$ = tolerance in the exit flow angle at Station 2
$\delta\dot{m}$ = tolerance in the mass flow rate at Station 2
ω = total pressure loss coefficient $(=(Pt_1\text{-}Pt_2)/Pt_1)$

Abbreviations

EXP = experiment
H_p = pressure side leg of horseshoe vortex
H_s = suction side leg of horseshoe vortex

Subscripts

1 = upstream position
2 = just downstream stator TE or rotor LE position
3 = far downstream of stator
ax = axial

References

[1] Klein, A., 1966, "Investigation of the Entry Boundary Layer on the Secondary Flows in the Blading of Axial Turbines," BHRA T1004.
[2] Langston, L. S., Nice, M. L., and Hooper, R. M., 1977, "Three-Dimensional Flow Within a Turbine Cascade Passage," ASME J. Eng. Power, **99**, pp. 21–28.
[3] Langston, L. S., 1980, "Crossflows in a Turbine Cascade Passage," ASME J. Eng. Power, **102**(4), pp. 866–874.
[4] Sieverding, C. H., and Van den Bosch, P., 1983, "The Use of Coloured Smoke to Visualize Secondary Flows in a Turbine-Blade Cascade," J. Fluid Mech., **134**, pp. 85–89.
[5] Sonoda, T., 1985, "Experimental Investigation on Spatial Development of Streamwise Vortices in a Turbine Inlet Guide Vane Cascade," ASME Paper No. 85-GT-20.
[6] Wang, H. P., Olson, S. J., Goldstein, R. J., and Eckert, E. R. G., 1997, "Flow Visualization in a Linear Turbine Cascade of High Performance Turbine Blades," ASME J. Turbomach., **119**, pp. 1–8.
[7] Deich, M. E., Zaryankin, A. E., Fillipov, G. A., and Zatsepin, M. F., 1960, "Method of Increasing the Efficiency of Turbine Stages With Short Blades," Translation No. 2816, Associated Electrical Industries Ltd., Manchester, England.
[8] Ewen, J. S., Huber, F. W., and Mitchell, J. P., 1973, "Investigation of the Aerodynamic Performance of a Small Axial Turbine," ASME Paper No. 73-GT-3.
[9] Morris, A. W. H., and Hoare, R. G., 1975, "Secondary Loss Measurements in a Cascade of Turbine Blades With Meridional Wall Profiling," ASME Paper No. 75-WA/GT-13.
[10] Kopper, F. C., Milano, R., and Vanco, M., 1981, "Experimental Investigation of Endwall Profiling in a Turbine Vane Cascade," AIAA J., **19**(8), pp. 1033–1040.
[11] Boletis, E., 1985, "Effects of Tip Endwall Contouring on the Three-Dimensional Flow Field in an Annular Turbine Nozzle Guide Vane: Part 1—Experimental Investigation," ASME J. Eng. Gas Turbines Power, **107**, pp. 983–990.
[12] Haas, J. E., 1982, "Analytical and Experimental Investigation of Stator Endwall Contouring in a Small Axial-Flow Turbine. 1—Stator Performance," NASA Report No. TP-2023.
[13] Moustapha, S. H., and Williamson, R. G., 1985, "Investigation of the Effect of Two Endwall Contours on the Performance of an Annular Nozzle Cascade," AIAA Paper No. 85–1218.
[14] 2000, *Evolutionary Computation 1: Basic Algorithms and Operators*, T. Baeck, D. B. Fogel, and T. Michalewicz, eds., Institute of Physics, University of Reading, Berkshire.
[15] Osyczka, A., 2002, *Evolutionary Algorithms for Single and Multicriteria Design Optimization*, Physica, Heidelberg.
[16] Hansen, N., and Ostermeier, A., 2001, "Completely Derandomized Self-Adaptation in Evolution Strategies," Evol. Comput., **9**(2), pp. 159–195.
[17] Farin, G., 1997, *Curves and Surfaces for Computer-Aided Geometric Design*, 4th ed., Academic, San Diego.
[18] Arima, T., Sonoda, T., Shirotori, M., Tamura, A., and Kikuchi, K., 1999, "A Numerical Investigation of Transonic Axial Compressor Rotor Flow Using a Low-Reynolds-Number k-ε Turbulence Model," ASME J. Turbomach., **121**, pp. 44–58.
[19] Wilcox, D. C., 1988, "Reassessment of the Scale-Determining Equation for Advanced Turbulence Models," AIAA J. **26**, pp. 1299–1310.
[20] Geist, A., Beguelin, A., Dongarra, J., Jiang, W., Mancheck, R., and Sunderam, V., 1994, *PVM: Parallel Virtual Machine: A Users' Guide and Tutorial for Network Parallel Computing*, MIT, Cambridge, MA.
[21] MPI: A message-passing interface standard, http://www-unix.mcs.anl.gov/mpi/
[22] Chien, J. Y., 1982, "Predictions of Channel and Boundary Layers With a Low-Reynolds-Number Two Equation Model of Turbulence," AIAA J., **20**, pp. 33–38.
[23] Sonoda, T., Arima, T., Olhofer, M., Sendhoff, B., Kost, F., and Giess, P.-A., 2006, "A Study of Advanced High Loaded Transonic Turbine Airfoils," ASME J. Turbomach., **128**, pp. 650–657.
[24] Hasenjäger, M., Sendhoff, B., Sonoda, T., and Arima, T., 2005, "Three Dimensional Aerodynamic Optimization for an Ultra-Low Aspect Ratio Transonic Turbine Stator Blade," ASME Paper No. GT2005–68680.

Downloaded 19 Dec 2008 to 202.33.79.26. Redistribution subject to ASME license or copyright; see http://www.asme.org/terms/Terms_Use.cfm